Characteristics of Suprathermal Electrons in Small-Scale Magnetic Flux Ropes and Their Implications on the Magnetic Connection to the Sun

Kyung-Eun Choi[1] · Dae-Young Lee[1] · Hee-Eun Wang[1] · Seunguk Lee[1] · Kyung-Chan Kim[1] · Kyung Sun Park[1]

Abstract

Small-scale magnetic flux ropes (SMFRs) are observed more frequently than larger-scale magnetic flux ropes (e.g., magnetic clouds) in interplanetary space. We selected 235 SM-FRs by applying cylindrical linear force-free fitting to 20-year observations of the Wind satellite, which meets the criteria of low beta, low temperature, an enhanced magnetic field, and a rotation feature. By examining the pitch angle distribution of suprathermal electrons for these events, we found that approximately 45.1% of the SMFRs were accompanied by unidirectional beams (strahl). A much smaller percentage of SMFRs (∼10.7%) were associated with bidirectional beams. We also found a small percentage (∼7.2%) of (sunward) conic distributions during SMFR events. Last, the remaining ∼37.0% of SMFRs were associated with complex electron distributions. The unidirectional beams and most of the conics (together corresponding to ∼50% of the total 235 SMFRs) imply open-field SMFRs with only one end connected to the Sun. For ∼37.7% of the unidirectional beam SMFRs, the local IMF field polarity was orthogonal or inverted (possibly due to interchange reconnection). Based on the solar wind conditions around the bidirectional beams, we suggest that more than half of the bidirectional beams were not necessarily closed-field-line SMFRs.

1. Introduction

The origin and characteristics of small-scale magnetic flux ropes (SMFRs) have been of interest in the community since the early reports by Moldwin et al. (2000) and Cartwright and Moldwin (2008). Moldwin et al. (2000) suggested that SMFRs originated not from the coronal region but at the heliospheric current sheet (HCS). Other studies suggested that SM-FRs could result from magnetic reconnection at the HCS (Feng, Zhao, and Wang, 2015; Sanchez-Diaz et al., 2019; Lavraud et al., 2020; Réville et al., 2020). Feng, Zhao, and Wang

✉ D.-Y. Lee
dylee@chungbuk.ac.kr

[1] Department of Astronomy and Space Science, Chungbuk National University, Cheongju, Chungbuk, Korea

(2015) investigated SMFRs involving counterstreaming electrons and whether they are associated with HCSs. They suggested that some SMFRs may be formed near HCSs. A series of blobs and flux ropes have been observed near sector boundaries (e.g., Sanchez-Diaz et al., 2019). A model has been proposed that describes the release of flux ropes by sequential magnetic reconnection at the tip of the helmet streamer (Sanchez-Diaz et al., 2019; Lavraud et al., 2020). Zeng and Hu (2018) compared the current density distributions inside SM-FRs between observational and numerical simulation results. Based on this, they suggested that SMFRs originate from self-generated solar wind turbulence. Additionally, Réville et al. (2020) showed that magnetic islands (flux ropes in dimension 3) can be generated over a whole range of scales in 2.5-dimensional MHD simulations from a sequence of tearing instabilities.

Some previous researchers examined small solar wind transients that may or may not be flux ropes (Kilpua et al., 2009; Yu et al., 2013, 2016). Kilpua et al. (2009) found that some small transients occur just at or close to the sector boundary during the solar cycle declining phase. Furthermore, they suggested that small transients have smaller expansion rates than ICMEs during the solar cycle minimum phase. Rouillard et al. (2011) reported evidence of magnetic transients with small radial extents ranging from 0.025 to 0.118 AU marked by low plasma beta values and short-timescale magnetic field rotations, all entrained by high-speed streams by the time they reach 1 AU. They suggested that these magnetic field structures originate as either small or large mass ejecta. Small-scale transients trapped inside corotating interaction regions (CIRs) can maintain their small size during propagation (Rouillard et al., 2009).

The methods used for identifying SMFRs have varied among researchers. Some have used force-free fitting modeling (Moldwin et al., 2000; Cartwright and Moldwin, 2008; Feng et al., 2008). Others have used more rigorous equilibrium modeling by solving the Grad–Shafranov equation (Hu et al., 2004, 2014, and 2018; Chen et al., 2020). Still others have identified solar transient events, some of which may be flux ropes and others not, simply based on characteristics of the solar wind parameters such as an enhanced magnetic field with rotation, reduced density and temperature (e.g., Kilpua et al., 2009; Yu et al., 2013, 2016). Most recently, magnetic and cross helicity-based techniques have been used to identify SMFRs when the Alfvenic nature of solar wind appears to be dominant (Zhao et al., 2020a, 2020b). Depending on the specific methods used, the identified SMFRs or small transients do not necessarily reveal the same statistical features, such as occurrence frequency and solar cycle dependence.

In the present work, we determine the characteristics of suprathermal electrons during SMFR events, which we selected by applying the cylindrical force-free model to the transient events published by Yu et al. (2016) obtained from Wind satellite observations from 1995 to 2014. We investigate the strahl of the suprathermal electrons during SMFRs to reveal the topological characteristics and their connection to the Sun. Examination of the pitch angle (PA) distribution of suprathermal electrons provides a hint regarding how the field lines are connected to the Sun compared to the IMF polarity. If the magnetic field lines are open with positive (negative) polarity, then suprathermal electrons ejected outward from the Sun along the field lines should appear as a unidirectional beam at a $0°$ ($180°$) PA. Closed field lines, however, are expected to exhibit counterstreaming electrons (bidirectional beam) at both $0°$ and $180°$ PAs departing from both ends of the field lines. Counterstreaming electrons have been used to identify usually closed-field structures of magnetic clouds. Feng, Zhao, and Wang (2015) identified SMFR events that indicate counterstreaming electrons (see Section 5 for comparison with our work here).

The present paper is arranged as follows. In Section 2, we briefly describe the way in which we select SMFRs with a force-free fitting model. In Section 3, we examine detailed

features of the suprathermal electrons during SMFR events and attempt to categorize them into different groups. In Section 4, we discuss the implications of suprathermal electrons on the global magnetic field structure of SMFRs. Finally, in Section 5, we summarize the main results and discuss a few issues.

## 2. Selection of Small-Scale Magnetic Flux Ropes

Yu et al. (2016) published a list of the small transient events (STs) in solar wind identified from the observations by the Wind, STEREO-A, and B spacecraft at 1 AU. Specifically, for the identification of STs, they adopted the following criteria: (i) duration between 0.5 and 12 hours, (ii) magnetic field strength higher than the yearly average, specifically by a factor of 1.3, (iii) low proton beta (β_p less than 0.7 times the yearly average) or low proton temperature (T_p/T_{exp} less than 0.7, where T_{exp} is the expected proton temperature for solar wind expansion each year), and (iv) low Alfvén Mach number (M_A less than 0.7 times the yearly average) or large rotation of the magnetic field components (for more detail, see Section 2.1 in Yu et al., 2016). It is important that they removed all the Alfvénic fluctuations from the list when the relation $\Delta V_\perp = \frac{\Delta B_\perp}{\sqrt{\mu_0 \rho}}$ is satisfied, where Δ represents the perturbation of the flow and field vectors relative to background, and $\perp$ means perpendicular to the background field. To define Alfvénic fluctuations quantitatively, they required the condition that either the correlations for three components of the flow speed and magnetic field vectors are greater than 0.5 or those for two components are greater than 0.6 and that for the other one is greater than 0.3. For the present work, we determined SMFRs from the Yu et al. ST list obtained from the Wind observations from 1995 to 2014 by applying the force-free fitting model (e.g., Shimazu and Vandas, 2002; Marubashi and Lepping, 2007; Lepping et al., 2011; Nishimura, Marubashi, and Tokumaru, 2019). Rigorously, force-free modeling is justified for $\frac{|\nabla P|}{|J \times B|} \sim \frac{\mu_0 P}{B^2} = \frac{\beta}{2} \ll 1$. To obtain a sufficiently large number of SMFR events for the statistical work designed in this work, we select SMFR events with a rather loose requirement that the average plasma beta based on protons is <1.

Figure 1 shows the solar wind conditions for an example SMFR along with the force-free fitting curves from the cylindrical model. The SMFR corresponds to $\sim$2 hours from 16:02 UT on 2004 September 14, as indicated by the two vertical lines. In the top panel, during the SMFR event, the magnetic field strength rises to more than 15 nT, and the magnetic field components rotate smoothly. This trend is reproduced in the fitting results (red curves). The solar wind speed is slow, $\sim$570 km/s, and steady in both the observation and the fitting results. The proton density, proton temperature, and plasma beta are reduced within the SMFR compared to those in the background. The blue line in the proton temperature panel denotes an expected proton temperature inferred from the solar wind speed derived by Yu et al. (2016). The last three panels show the magnetic field vector variation as seen by the spacecraft passing through the flux rope. Eventually, the number of SMFRs successfully determined by force-free modeling (satisfying a least-mean squared error less than 0.3) is 261 out of the 1067 ST events in the original Yu et al. list from the Wind observations.

3. Classification and Characteristics of Suprathermal Electrons

In this section, we determine the characteristics of the suprathermal electrons during the SMFR intervals selected in the previous section to provide some hints regarding the SMFR

Figure 1 An example SMFR. Solar wind plasma and magnetic field data from the Wind satellite during ∼8 hours on 14 September 2004. From top to bottom are the IMF *B* and GSE components, solar wind speed, proton density, proton temperature, plasma beta, and magnetic field vectors. The vertical lines denote the boundaries of the SMFRs. The red lines present the results of least-squares fitting.
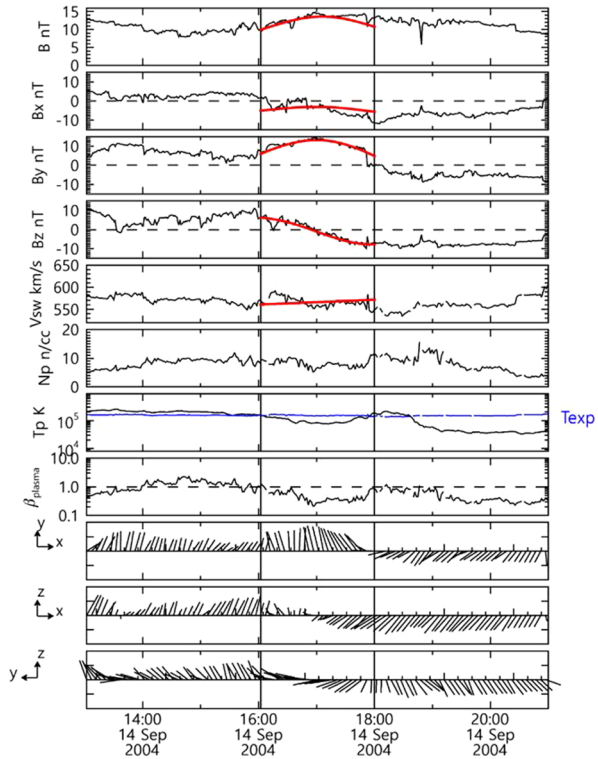

field line topology, in particular, whether the SMFR field lines are open or closed, as discussed in the next section. For this purpose, we use suprathermal electron flux data from 3D plasma analyzer (3DP) (Lin et al., 1995) observations made onboard the Wind spacecraft. 3DP provides the PA distributions of electrons at energies from a few eV to hundreds of keV. We use the PA distribution flux data at energy centered at ∼260 eV. These data are available for 235 SMFR events out of the 261 SMFRs identified in the previous section. For these 235 SMFRs, we determine the cases where the electron flux exhibits a unidirectional beam at either a 0° or 180° PA (usually known as "strahl"), those where the electron flux exhibits a counterstreaming beam in addition to the strahl (we call them "bidirectional beams" in this paper), and the conics that are characterized by an electron flux enhancement over a limited PA range off the magnetic field direction in addition to the usual strahl (thus distinguished from bidirectional beams).

3.1. Classification

Classification of the electron flux beam structure is nontrivial since the electron flux structure often appears complex, and there is no exclusive way, based solely on physics, to set quantitative criteria to define the flux beam patterns. Nevertheless, in the present study, we attempt to categorize the electron flux patterns among SMFRs by the following procedures.

3.1.1. Unidirectional Beams

First, for the unidirectional beam events, (i) we first exclude the cases where a counterstreaming beam or conic beam is clearly identified by visual inspection and all other cases
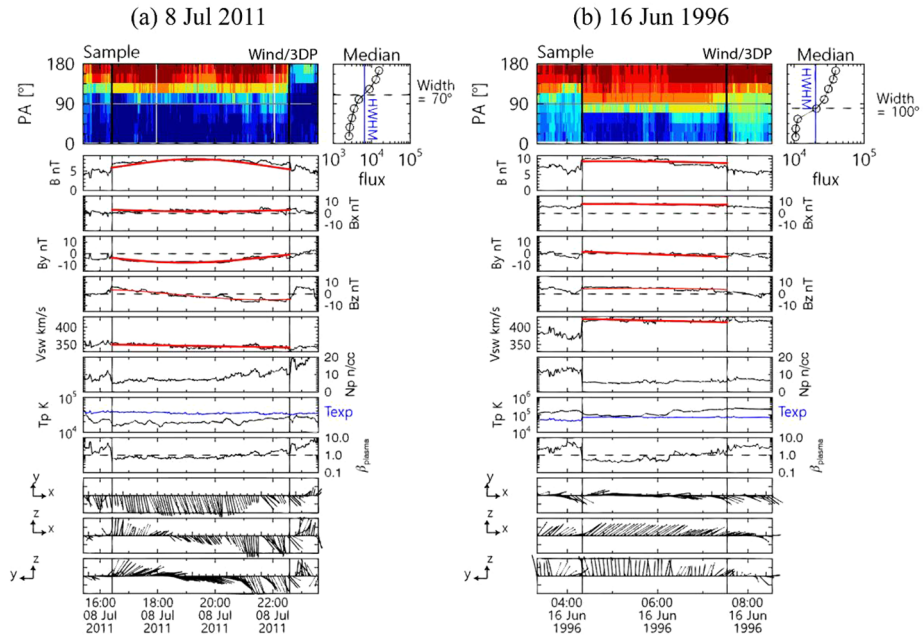
Figure 2 Two examples of SMFR events (intervals marked by black vertical lines) identified by applying the force-free fitting model (red curves). These are distinguished by different widths of the 260 eV electron beams (top panels). (**a**) An example that is identified as a unidirectional beam event and (**b**) an example that is excluded from the unidirectional beam event group. In the top panels, the color scales for the electron fluxes in two events range from 3.0×10^3 to 1.5×10^4 s^{-1} cm^{-2} sr^{-1} eV^{-1} and from 9.0×10^3 to 3.8×10^4 s^{-1} cm^{-2} sr^{-1} eV^{-1}. On the right side of each top panel, the median flux profile is shown (the horizontal and vertical axes refer to the electron flux and pitch angle, respectively, and the blue vertical line indicates the half-width at half maximum (HWHM)). The data in the second to bottom panels are shown in the same format as in Figure 1.

where the flux distribution in the PA and time appears too complex to be classified. (ii) Then, out of the events selected in step (i), we require a specific threshold condition in which the median flux difference between the 0° and 180° PA sides is ≥2.5 for an event to be considered a unidirectional beam event. This threshold value of 2.5 is rather arbitrary, but we have chosen this empirically after checking the overall statistical distribution of flux differences between the two PAs for all SMFR events, from which we found that 2.5 appears to be a reasonable threshold value to identify a unidirectional beam situation. (iii) Furthermore, we require that the beam width for each PA be ≤80°, where the beam width is defined as the "half width at half maximum (HWHM)". We use the beam width requirement to exclude beam cases that are too broad.

Figure 2 shows an example of the identified unidirectional beam events (column (a)) and an example of the excluded events (column (b)). We define the "HWHM beam width" in the pitch angle distribution from the median flux profile in PA during the SMFR period, as shown in the top rows in Figure 2. As a selection criterion for the unidirectional beams, we reject the cases of beam width >80° and categorize them as unclassified events. The beam width of the event in column (a) is 70° and thus meets the beam width criterion for the unidirectional beams. In contrast, in the event on column (b), whereas the major beam exists at the PA = 180° side, a substantial electron flux exists around PA = 90° such that

the HWHM beam width is 100°. Accordingly, this kind of SMFR event is not selected as a unidirectional beam event. Based on this procedure, we identify a total of 106 events as unidirectional beam events out of a total of 235 SMFRs.

3.1.2. Bidirectional Beams

The classification of bidirectional beam events is more difficult for a few reasons. First, when a type of bidirectional beam appears to exist, it is not necessarily always continuous and uniform throughout the SMFR period. Bidirectional beams are often intermittent and exist for a limited amount of time. From a practical viewpoint for bidirectional beam event identification, the extent to which a beam flux is allowed to not be continuous throughout the SMFR interval must be specified. Second, the bidirectional beam structure is often asymmetric between the two PA sides (0° and 180° PA). The asymmetry can occur in flux intensity, beam width, or beam duration. One reason for this is that the spacecraft does not necessarily cross the central part of the entire flux tube. Gosling, Teh, and Eriksson ([2010](#)) pointed out that the electron strahl intensity can vary as a function of distance from the Sun along the field line such that a spacecraft crossing a part of the flux tube well away from the central part will observe stronger electron intensity at one PA side than at the opposite PA side. Additionally, magnetic mirroring by a higher field region and/or wave-driven scattering effect may occur more dominantly on one PA side. The extent to which one can allow PA asymmetry should be set for bidirectional beam event identification. Last, some bidirectional beams may appear to exist due to the 90° depletion effect, regardless of whether the associated field is open or closed (Gosling, Skoug, and Feldman, [2001](#); Gosling et al., [2002](#)). This phenomenon may be difficult to distinguish from "true" bidirectional beams. True beams may be identified more clearly if the flux is enhanced compared to the flux level prior to the SMFR start time, regardless of whether the 90° depletion coexists.

Considering the difficulties stated above, we identify the bidirectional beam events as follows. (i) Based on a visual inspection, we first identify the "background" beam at either 0° or 180° that exists continuously at an approximately similar level prior to and during the SMFR event (most of its time). Then we check whether the "counterstreaming" beam on the opposite PA side exists, where flux enhancement occurs at the beginning or at least sometime during each interval (i.e., enhanced flux relative to a prior time). Without the counterstreaming beam, the background beam flux alone may be classified as a unidirectional beam event if it satisfies the unidirectional beam selection criteria described above in Section [3.1.1](#) (ii) We distinguish bidirectional beam events from conic events, the flux peak of which occurs at PA away from 0° or 180°, and separately classify them in Section [3.1.3](#) (iii) We avoid any bidirectional beam-like events that are suspicious and simply due to the 90° depletion effect. For this to be done safely, we impose a conservative condition that the flux on at least one side of the PA should increase at or during the SMFR event compared to the flux at a prior time so that the identified bidirectional beam is not simply due to 90° depletion. Based on this selection procedure, we identify a total of 25 bidirectional beam events out of a total of 235 SMFRs.

Figure [3](#) shows two examples of SMFR showing enhanced electron fluxes at both PA = 0° and 180° sides. In the event in column (a), whereas the strahl exists at PA = 0° nearly throughout the SMFR interval, the counterstreaming beam at PA = 180° with a larger flux level than the strahl exists in the middle of the SMFR interval. We identify this kind of event as a bidirectional beam event. In contrast, in the event in column (b), electron beams exist at both PA = 0° and 180°, but at the same time, there is a notable flux depletion around PA = 90°. The apparently bidirectional beam feature in this event could be affected by the
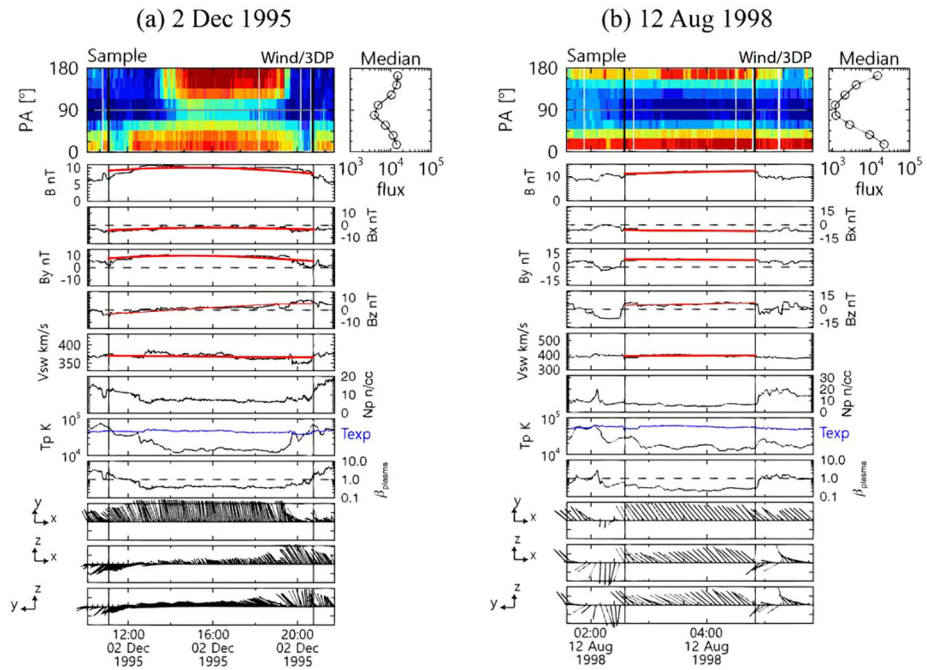
Figure 3 Two examples of SMFR events showing 260 eV electron beams. (**a**) An example that is identified as a bidirectional beam event and (**b**) an example that is excluded from the bidirectional beam event group. All the data are shown in the same format as in Figure 2.

90° depletion effect, and we decide not to include this kind of event as a bidirectional beam event.

To supplement the identification of the bidirectional beam events from steps (i) to (iii), we quantitatively determine the temporal continuity and the asymmetry in the PA (i.e., the extent to which the identified bidirectional beam feature is symmetric between the two PA sides). We demonstrate this in Figure 4 for the bidirectional beam event shown in column (a) of Figure 3 (repeated in Figure 4a). Here we define the 0° PA beam as the background beam (the strahl) and the 180° PA beam as the counterstreaming beam. Figure 4b shows the line plots of the background beam (j_b, red) and counterstreaming (j_c, blue) fluxes with $\langle j_b \rangle$ (green), which is the average of the background beam flux during the SMFR period. We define "j_{ratio}" as the flux ratio of j_c to $\langle j_b \rangle$, that is, the counterstreaming flux level relative to the average background beam flux level. Using this ratio, we attempt to quantitatively determine the extent to which the counterstreaming beam differs in flux level and duration from the average background flux during the chosen event interval. If j_{ratio} is 100% for the entire time interval for a given event, then this bidirectional beam is mostly symmetric between the two opposite PA sides. Any bidirectional beam would be considered to be more asymmetric if j_{ratio} were too small or large for a long time interval. Figure 4c shows the line plot of j_{ratio} for the event in Figure 4a. j_{ratio} is mostly close to 100% in this event. In particular, the shaded area refers to the time interval when j_{ratio} lies between the two dashed horizontal lines denoting 90% and 110%, respectively. The total time fraction (T_{fraction}) of this shaded interval is ∼63% of the SMFR duration, that is, for this event, the bidirectional beam is nearly symmetric for ∼63% of the event time.
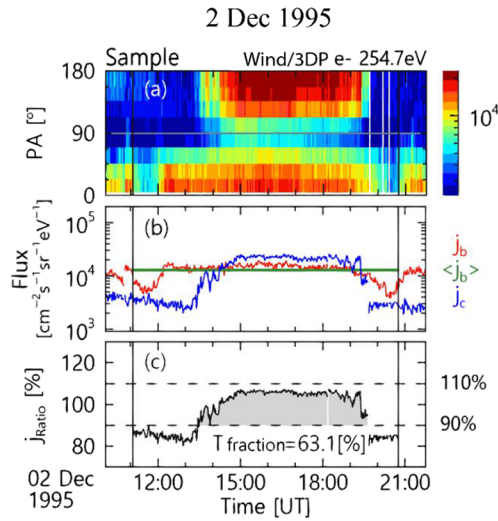
Figure 4 The analysis method of beam flux symmetricity for the bidirectional beam SMFR shown in Figure 3a. (**a**) Pitch angle distribution of a sample bidirectional beam event (interval defined by vertical black lines), the same data as the top panel in Figure 3a, repeated here for convenience. The color denotes flux levels ranging from 2.3×10^3 to 2.3×10^4 s^{-1} cm^{-2} sr^{-1} eV^{-1} on the logarithmic scale. (**b**) The background beam flux j_b (red; the beam flux at pitch angle = 0°), its average over the SMFR period, $\langle j_b \rangle$ (green), and the counterstreaming beam flux j_c (blue; the flux at pitch angle = 180°). (**c**) The flux ratio of j_c to $\langle j_b \rangle$, (j_{ratio}). The gray area refers to the time fraction (T_{fraction}) of the event interval satisfying the criterion 90% $\langle j_{\text{ratio}} \rangle$ 110%, representing the degree of symmetricity of the beam fluxes between opposite pitch angle sides.

3.1.3. Conics

As distinguished from the bidirectional beam type, we identify conics that occurred during SMFRs. For this type of SMFR event, whereas a well-defined (antisunward) strahl structure was observed at one side of the PA directions, either 0° or 180°, conics occurred on the opposite side of the strahl (thus sunward) over a limited PA range off the magnetic field direction. An example event is shown in Figure 5, where the antisunward strahl exists at PA = 0° (black arrow on the left side of the top panel), and the conics of a weaker flux intensity exist most obviously at PA = 112°–135° (white arrow in the top panel, also marked in the median flux profile). In total, we identify conics for 17 SMFR events, the details of which are described in Section 3.2.
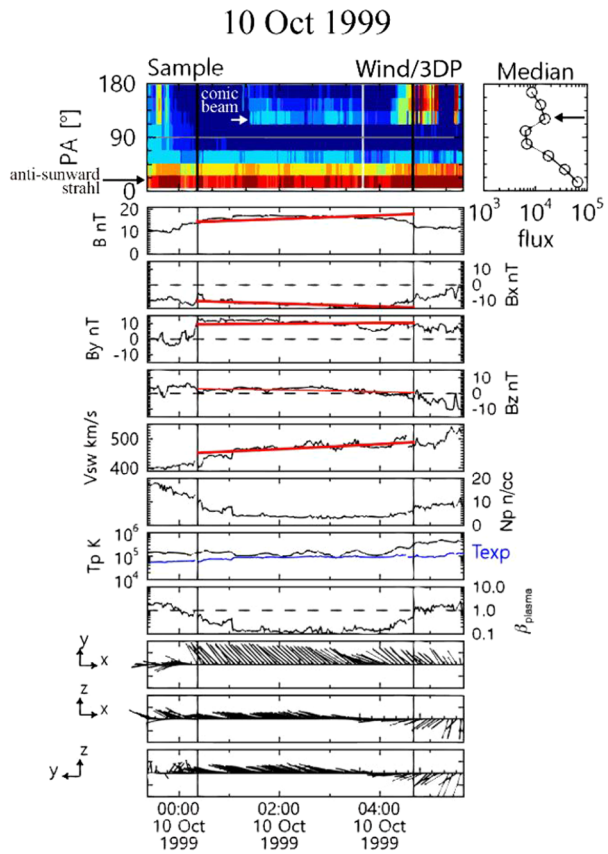
3.2. Statistical Features

Table 1 summarizes the statistics of the identified electron flux patterns. The unidirectional beam type is the largest population, constituting 45.1% of the total, the bidirectional beam type exists for 10.7% of the SMFRs, and the conic-type events are the smallest population, constituting 7.2%. A substantial fraction of SMFR events, that is, 37%, exhibit complex electron flux patterns, which could not be classified.

Figures 6–8 and Tables 2–4 provide summaries of various information for the unidirectional beam, bidirectional beam, and conic-type events separately. First, Figure 6 summarizes the statistics of the beam width (as described in Figure 2 and Section 3.1.1) and flux ratio between PA = 0° and 180° together for the 106 unidirectional beam events. These

Figure 5 An example of SMFR showing conics in electron PA distribution shown in the same format as in Figure 2. The black arrow on the left side of the top panel indicates the antisunward strahl, whereas the white arrow denotes conics (also indicated by the black arrow in the median flux plot).
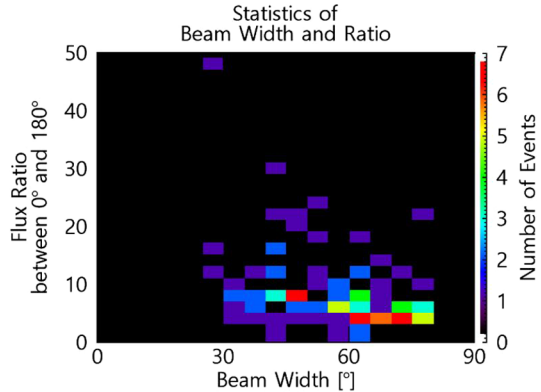

Table 1 Statistics of SMFRs as classified by the pitch angle distribution of suprathermal electrons.

| Group	Number of SMFRs (ratio)
Unidirectional beam	106 (45.1%)
Bidirectional beam	25 (10.7%)
Conics	17 (7.2%)
Unclassified	87 (37.0%)
Total	235

specific numbers are included in Table 2, which also contains other information for all 106 unidirectional beam events (further discussion is given in Section 4.1). Clearly, rather broad beam cases are frequent, and the majority of the unidirectional beam events correspond to flux ratios between a few to <10.

Figure 7 shows the statistics of the time fraction for each of the 25 bidirectional events that satisfies the condition $90\% < j_{ratio} < 110\%$, which is intended to represent a symmetric bidirectional beam situation (as described in Figure 4 and Section 3.1.2). Overall, the majority of the identified bidirectional beams are more or less characterized by a symmetric bidirectional beam. Specifically, 18 out of 25 events meet the symmetry condition for the time fraction of >60%. Table 3 includes the specific time fraction of each event satisfying
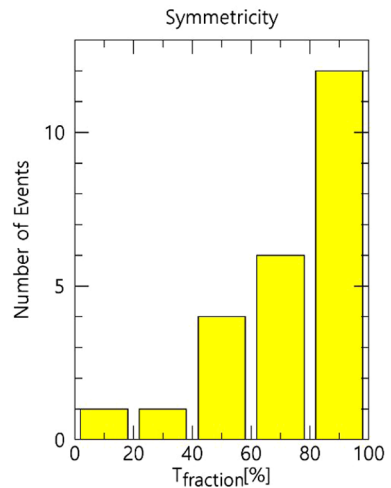
the symmetricity requirement used for Figure 7. Table 3 also provides other information, which is discussed in Section 4.2.

Figure 8 shows the flux curves versus PA for the 17 conic type events with the convention that the horizontal axis refers to PA from the strahl side. They are fluxes at each PA averaged over the time intervals in which the conical beam occurred during SMFR events. Clearly, the conic beam peak occurs between ~120° and ~150°, thus off the magnetic field direction. We further estimate the conic beam flux ratio relative to the strahl flux. Table 4 includes this ratio for all 17 conic-type events, and on average, this flux ratio is 0.2, that is, the conic beam flux is not very strong on average, except for some events (as marked by the numbers in Figure 8), which are further discussed in Section 4.3. Additionally, nearly all 17 conic events are accompanied by the 90° depletion effect (Gosling et al., 2001, 2002). More discussion on the information in Table 4 is given in Section 4.3.

Finally, we use another statistical method to demonstrate the validity of the identification of the beam flux types done in Section 3.1. Specifically, following the method by Feuerstein et al. (2004), we show in Figure 9 the distribution of the beam flux ratio to halo electron flux separately for all 235 events, 106 unidirectional beam events, and 25 bidirectional beam events. For the halo electron flux, we take the flux at PA = 90°. The distributions of the uni-

Table 2 List of characteristics of unidirectional beam-type SMFRs.

| No.	Start time (yyyymmdd hh:mn)	Duration (hour)	Beam pitch angle (°)	Beam width (°)	Beam flux ratio	Sector crossing time (day)
1	19950619 08:28	2.2	0	65	13.5	−0.16
2	19961104 02:40	1.8	0	75	4.6	−0.08
3	19961209 22:00	1.3	0	70	3.3	−0.84
4	19970921 09:35	5.0	0	45	8.0	
5	19980723 03:48	1.0	0	50	9.8	−2.08
6	19981015 11:30	3.1	180	45	7.5	−1.37
7	19990806 10:40	1.6	0	70	6.7	−0.60
8	20000416 07:10	2.8	0	55	7.1	−0.08
9	20000513 03:10	2.3	0	45	8.6	−0.72
10	20000615 00:28	1.1	0	65	9.2	
11	20000930 19:35	4.2	0	40	29.2	
12	20001005 03:30	2.9	0	60	5.0	
13	20010104 10:00	1.2	0	40	8.8	−0.26
14	20010408 16:00	5.4	180	25	16.3	−0.35
15	20010716 05:30	3.8	0	35	12.0	−2.01
16	20010817 13:48	4.5	0	50	17.5	
17	20021214 17:20	2.7	180	25	47.2	
18	20021219 11:25	2.3	0	75	22.3	−0.43
19	20021223 01:12	3.0	0	25	12.8	
20	20021226 11:45	4.7	0	40	11.8	
21	20030109 17:35	5.2	180	75	9.1	
22	20030408 06:48	0.8	0	40	4.8	−0.68
23	20030714 17:55	4.2	180	70	4.8	−3.32
24	20030901 11:30	7.2	180	45	7.6	−0.36
25	20030909 02:38	2.3	180	45	21.2	
26	20040309 20:32	1.5	180	35	8.2	−0.30
27	20040905 17:22	5.4	0	45	19.8	−0.83
28	20040914 16:02	2.0	0	45	4.6	−0.54
29	20050316 14:22	11.4	180	55	9.8	−0.28
30	20050317 11:25	2.2	180	45	7.4	−1.15
31	20050404 12:35	1.5	180	50	11.8	−2.68
32	20050430 02:45	3.8	180	45	5.9	−0.97
33	20050507 21:22	1.0	180	70	3.3	−0.02
34	20050604 21:05	1.3	180	60	11.5	−0.59
35	20051129 22:15	1.1	180	60	4.4	−1.59
36	20051130 01:18	1.7	180	35	5.4	−1.71
37	20060220 05:00	1.3	180	65	3.0	−1.33
38	20060310 04:35	2.4	0	55	5.7	−1.45
39	20060704 17:30	3.8	180	70	6.3	−0.41
40	20060910 21:30	4.3	180	60	5.2	−0.57
41	20070102 06:25	1.6	0	35	4.3	−0.82

Table 2   (*Continued*)

No.	Start time (yyyymmdd hh:mn)	Duration (hour)	Beam pitch angle (°)	Beam width (°)	Beam flux ratio	Sector crossing time (day)
42	20070115 11:00	1.4	0	60	4.2	−0.00
43	20070306 05:28	1.0	180	60	11.6	−2.46
44	20070402 12:18	0.6	180	30	4.1	−1.69
45	20070422 21:45	1.3	0	75	6.0	−0.44
46	20070614 11:25	2.1	0	60	4.5	−0.84
47	20070726 18:32	0.8	0	65	3.4	−0.43
48	20070729 12:05	3.2	180	60	6.6	−0.83
49	20080105 06:20	0.8	180	60	4.0	−0.65
50	20080113 13:30	1.6	0	60	7.9	−1.27
51	20080210 06:22	3.1	0	55	8.5	−2.36
52	20080606 08:55	2.4	180	60	18.2	−0.37
53	20080615 18:22	2.1	180	30	7.6	−1.50
54	20090119 06:05	1.7	180	60	6.9	
55	20090313 02:00	1.0	180	65	4.4	−0.01
56	20090321 20:30	3.0	0	65	5.2	−2.05
57	20090806 09:17	1.5	180	60	3.1	−0.91
58	20090819 23:05	2.3	180	55	5.2	−2.61
59	20090904 00:10	2.5	180	75	3.6	
60	20100111 13:50	0.9	180	55	3.0	−0.63
61	20100301 10:00	3.5	180	75	5.0	−0.41
62	20100310 14:15	2.4	180	65	8.1	
63	20100326 20:38	1.4	0	4	11.8	−1.42
64	20100326 22:20	3.6	0	40	16.5	−1.49
65	20100331 23:15	2.0	0	45	7.8	−2.52
66	20100914 20:50	1.5	0	60	2.5	0.63
67	20101019 07:20	4.8	180	60	7.0	−0.64
68	20101022 15:50	3.5	180	50	6.4	
69	20101022 21:40	3.9	180	45	5.3	
70	20101111 01:00	2.1	0	65	4.5	1.45
71	20101127 20:15	3.2	0	40	2.8	0.65
72	20101225 19:18	4.0	0	70	4.0	−2.05
73	20110103 20:42	1.3	0	65	4.5	−0.30
74	20110214 20:50	5.5	0	70	6.4	−0.36
75	20110412 05:12	3.7	0	30	8.2	−0.88
76	20110607 18:45	3.9	180	70	12.4	
77	20110609 19:22	2.6	180	60	7.6	1.67
78	20110708 16:25	6.2	180	70	6.0	0.07
79	20110814 09:40	2.0	180	60	3.0	−0.96
80	20110814 23:40	0.9	180	35	5.9	−1.50
81	20111220 04:05	2.6	0	70	3.0	−0.75
82	20120116 10:15	3.1	180	75	4.9	−1.41
83	20120122 11:40	5.8	180	70	4.2	2.26

Table 2 (*Continued*)

No.	Start time (yyyymmdd hh:mn)	Duration (hour)	Beam pitch angle (°)	Beam width (°)	Beam flux ratio	Sector crossing time (day)
84	20120130 16:02	1.5	0	60	2.7	2.30
85	20120213 09:40	6.4	180	70	3.3	−0.23
86	20120630 02:18	1.8	180	55	5.6	−0.32
87	20120630 06:38	1.0	180	65	4.2	−0.50
88	20120802 14:28	4.5	180	55	10.0	3.05
89	20120813 09:30	3.3	180	40	21.7	−1.07
90	20120926 12:30	3.0	180	55	6.0	2.43
91	20121217 06:58	1.5	0	35	7.4	
92	20121217 13:35	4.9	0	50	6.2	
93	20130126 13:40	2.9	180	40	7.8	−1.53
94	20130218 23:25	3.2	0	75	5.9	1.25
95	20130314 02:48	5.3	0	60	8.2	2.87
96	20130320 19:50	3.8	180	40	7.9	3.13
97	20130620 22:30	2.5	180	50	4.2	
98	20140121 19:35	5.7	0	50	23.4	−3.09
99	20140207 23:00	0.8	180	55	5.3	0.33
100	20140213 08:58	1.2	180	75	3.4	0.70
101	20140223 21:22	1.8	0	45	7.7	
102	20140318 19:48	0.9	180	75	5.8	−0.81
103	20140407 17:00	1.3	0	30	5.3	
104	20140617 19:02	2.7	180	40	17.0	−0.31
105	20140728 10:25	1.0	180	55	3.2	−0.30
106	20140810 13:00	5.1	180	30	9.5	−0.32

Figure 8 Pitch angle distribution of electron fluxes for the 17 conic-beam-type events. The red line depicts the average flux profile. The four numbers 2, 4, 8, and 14 refer to the event identification numbers listed in Table 4 and represent conic events with relatively large flux peaks.
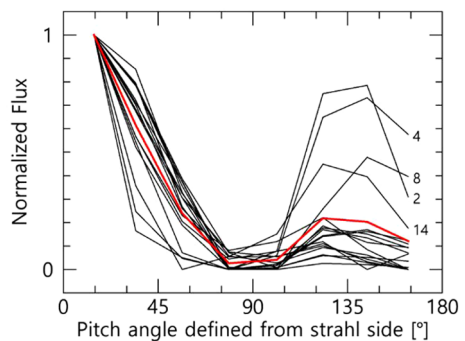
directional beam and bidirectional beam groups in Figures 9b and 9c are well distinguished from each other. The majority of unidirectional beam events lie well off the diagonal line such that the flux ratio of the 0° pitch angle is larger than that of the 180° PA (and vice versa), justifying the unidirectional beam nature. The unidirectional beam flux ratio lies mostly from 2 to 10, implying that the beam flux intensity is well distinguished from the

Table 3 List of characteristics of bidirectional beam-type SMFRs.

No.	Start time (yyyymmdd hh:mn)	Duration (hour)	Symmetric beam rate[a] (%)	Bow shock[b] (%)	Solar wind event[c]	Sector crossing time (day)
1	19951202 11:05	9.67	63.1	0.0		1.78
2	19980731 18:32	2.63	90.6	0.0	Downstream of IPS	
3	19990211 20:22	1.63	100.0	0.0	Inside CIR	−0.40
4	19991121 19:05	0.75	7.1	0.0		0.28
5	20020108 06:35	0.97	94.3	0.0		−0.05
6	20020417 17:45	0.67	70.8	0.0	Sheath ahead of ICME	2.52
7	20040818 08:02	4.38	50.0	0.0	Trail of ICME	0.41
8	20050219 05:50	2.83	74.0	33.5	Trail of ICME[d]	
9	20050910 01:45	2.33	100.0	7.1	Leading edge of HSS	−0.26
10	20060310 17:26	2.10	83.3	86.5	Leading edge of HSS	−1.99
11	20080606 23:38	4.03	71.6	0.0	Ahead of CIR	−0.98
12	20100211 11:30	10.87	76.9	0.0	Downstream of IPS	
13	20110204 18:40	1.42	100.0	0.0	Inside CIR	
14	20110406 09:10	2.20	63.0	27.3	Downstream of IPS	
15	20110711 18:42	3.50	31.5	59.0	Leading edge of HSS	−2.77
16	20110926 20:55	3.25	78.6	20.5	Leading edge of HSS	−0.61
17	20111009 13:30	2.77	23.8	6.6		
18	20120331 14:22	2.38	100.0	0.0		
19	20131029 16:38	0.87	100.0	0.0		0.76
20	20131129 15:52	1.30	97.8	0.0		−2.67
21	20140227 20:42	2.80	100.0	0.0	Inside CIR	−0.43
22	20140407 09:28	1.78	100.0	0.0		
23	20140505 03:00	8.58	96.7	0.0		0.50
24	20140603 00:45	1.42	100.0	0.0		1.16
25	20140917 20:45	2.08	60.0	0.0		

[a]Temporal percentage that satisfies a symmetric beam condition (see text in Section 3.1.2).

[b]Time ratio that satisfies the cone angle within 20 degrees between two vectors of the local magnetic field vector and spacecraft-to-Earth (see Section 4.2).

[c]Solar wind structures associated with SMFRs (see Section 4.2).

[d]Alternatively, it may be associated with a leading edge of HSS (see Section 4.2).

halo electron flux level. In contrast, Figure 9c indicates that the majority of bidirectional beam events exist around the diagonal line such that the flux ratios of the two PAs are comparable to each other, justifying the nature of the identified bidirectional beam events. However, although most of the bidirectional beam events are associated with the flux ratio

Table 4 List of characteristics of the conic-beam-type SMFRs.

No.	Start Time(yyyymmdd hh:mn)	Duration (hour)	Beam pitch angle (°)	Conic flux ratio[a]	Bow shock[b] (%)	Solar wind Event[c]	Sector crossing time (day)
1	19950103 00:25	1.8	180	0.13	42.9	Inside CIR	−0.96
2	19950803 06:22	1.1	0	0.89	50.0		−2.58
3	19981015 19:20	3.2	180	0.14	6.8		1.25
4	19981130 10:05	8.3	180	0.83	54.5		0.30
5	19990811 01:05	2.0	180	0.46	0.0		−0.46
6	19991010 00:22	4.3	0	0.25	15.9	Inside CIR	−0.50
7	20011105 03:00	5.5	180	0.31	56.1		−2.53
8	20050118 17:10	1.3	0	0.57	1.3	Trail of ICME	−1.78
9	20050821 15:40	8.1	0	0.41	43.1		−0.12
10	20071110 01:20	2.0	180	0.45	55.0	Leading edge of MSS	
11	20080131 21:55	5.0	180	0.37	67.0	Leading edge of HSS	−0.57
12	20100216 03:40	7.8	0	0.31	1.3		−0.26
13	20100412 19:35	3.3	0	0.30	0.0	Immediately after ICME	−0.22
14	20100803 17:22	2.0	180	0.76	0.0	Downstream of ICME-shock	
15	20111220 14:35	3.9	180	0.37	38.0		−1.19
16	20130425 08:55	0.7	180	0.61	0.0	Leading edge of HSS	−1.61
17	20130917 19:20	2.0	0	0.52	0.0		−0.13

[a]Peak flux of the conic beam relative to the strahl flux.

[b]Time ratio that satisfies the cone angle within 20 degrees between two vectors of the local magnetic field vector and spacecraft-to-Earth (see Section 4.3).

[c]Solar wind structures associated with SMFRs (see Section 4.3).

range of ∼1–4 on both PA sides, the flux ratio for some of the bidirectional beam cases is close to 1, implying that the beam flux is comparable to the halo electron flux at a 90° pitch angle. This phenomenon occurs because for some of the bidirectional beam events, the well-known heat flux dropout effect occurs, and these data points contribute to the beam flux to halo electron flux ratio being equal to unity in Figure 9c. Overall, we believe that the results in Figure 9 facilitate verification of the effectiveness of our selection method for the unidirectional beam and bidirectional beam events done in Section 3.1. However, the method in Figure 9 is not useful for conic-type events.

4. Implications on SMFR Field Line Structure and Connection to the Sun

Our selection procedure leads us to conclude that the unidirectional beam strahl is dominant for the majority of SMFRs. This result implies that the majority of SMFRs are open-field flux ropes connected to the Sun at only one end. In contrast, bidirectional beam-type events
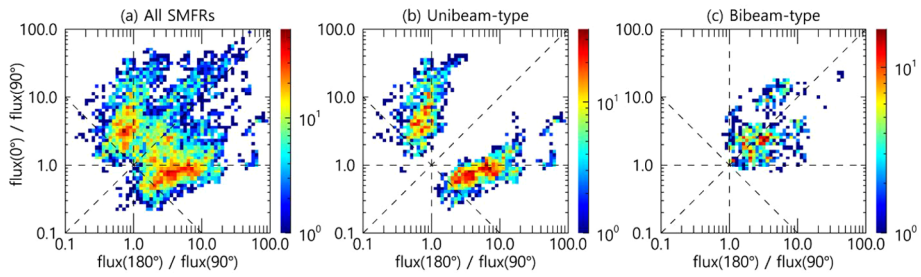
Figure 9 Directional distribution of the flux of the suprathermal electron strahl data (pitch angle = 0° or 180°) compared with that of the halo data (pitch angle = 90°). For (**a**) all events, (**b**) the unidirectional beam, and (**c**) the bidirectional beam SMFRs selected from our criteria in this work. The color bar shows the number of data sets.

possibly imply a closed-field structure, but several factors must be carefully considered before we make a firm conclusion, as discussed later in this section.

4.1. Implications from Unidirectional Beams

The open fields inferred from the unidirectional beam can be further distinguished by their polarity, that is, either toward or away from the Sun. We determine the "solar polarity" of an SMFR from the electron beam direction relative to the local IMF (SMFR) polarity. By "solar polarity" we mean the direction of the magnetic field inferred from the electron beam direction when the SMFR field line is mapped to the solar surface. Specifically, if the electron beam in the interplanetary space is observed at PA = 0° (180°), then it implies that the corresponding field polarity at the Sun, that is, the solar polarity, is supposed to be "away" from ("toward") the Sun. The solar polarity can be inconsistent with the local SMFR polarity if the interplanetary field is deformed. Figure 10 illustrates two situations where the solar polarity inferred from the electron beam pitch angle (away) is consistent with the local field polarity in case (a), whereas two polarities are opposite due to the locally inverted field shape (Owens, Crooker, and Lockwood, 2013) in case (b).

Table 5 shows the statistics of the solar polarities for the unidirectional beam SMFRs in the first two rows. There is only a modest difference between two senses of solar polarity such that the "toward" polarity case is more frequent by ~10% point than the "away" polarity case. The reason for this small difference is unclear to us at present. The statistics of the comparison of the local IMF polarity with the solar polarity are also shown in Table 5. For simplicity of the analysis, we have estimated an average polarity of the magnetic field during each SMFR, which represents an overall polarity sense. For ~37.7% of the unidirectional beam SMFRs, the local IMF polarity does not match the solar polarity, being either inverted (possibly due to interchange reconnection (Owens, Crooker, and Lockwood, 2013)) or orthogonal (more frequently). This result means that the global structure of the unidirectional beam SMFR field lines connected to the Sun is not necessarily simple and could be distorted during propagation.

4.2. Implications from Bidirectional Beams

The most likely implication inferred from the bidirectional beam events is that the SMFRs are closed-field flux ropes. However, the counterstreaming strahl in the bidirectional beam cases can be seen in satellite observations due to reasons other than the closed-field

Figure 10 Schematics demonstrating the solar field polarity (Solar **B**) inferred from the electron beam direction (red arrow) measured by interplanetary spacecraft (green circle) in comparison with the local interplanetary field polarity (Local **B**).

	Case (a)	Case (b)
Observed local field polarity	Away	Toward
Expected e- beam pitch angle	0˚	180˚
Observed e- beam pitch angle	0˚	0˚
Inferred solar field polarity	Away	Away
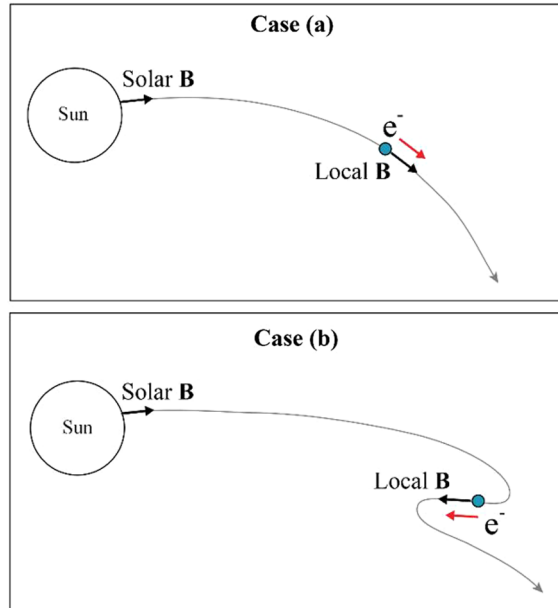
Table 5 Statistics of solar polarity inferred from unidirectional beam strahl and comparison with local IMF polarity.

Solar polarity	Number (ratio)
Away	47 (44.3%)
Toward	59 (55.7%)

Local IMF polarity	Number (ratio)
Same as solar polarity	66 (62.3%)
Opposite to solar polarity (inverted)	6 (5.7%)
Orthogonal	34 (32.0%)

structure. Wimmer-Schweingruber et al. (2006) suggested, as possible origins for bidirectional electrons generated on open field lines at 1 AU, electrons streaming from the Earth's bow shock (Stansberry et al., 1988), electron reflection from interplanetary shocks (Gosling et al., 1993), mirroring from compressed magnetic fields (Gosling et al. 2001), and temperature anisotropy in the core electrons due to a low plasma density (Philips and Gosling, 1990). In these cases the field lines do not have to be closed.

We have investigated the possibility that the bidirectional beam electrons of our SMFRs are due to back-streaming from the Earth's bow shock. Feldman et al. (1982) reported that back-streaming electrons from the bow shock are often detected at ISEE-3 when the cone

Figure 11 Schematics demonstrating possible bidirectional beams under an open field structure.
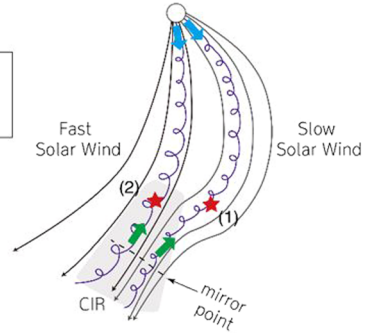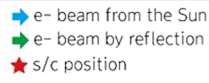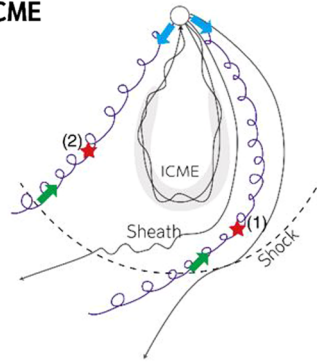

angle between the local magnetic field vector and the spacecraft-to-earth vector is within ~20° from the spacecraft–Earth line. We have determined the "time ratio of the bow shock connection" satisfying this criterion used in Feldman et al. (1982), representing how long the connection is maintained between the Wind magnetic field and the bow shock during the SMFR intervals. The results are given in Table 3, which indicate that most of the bidirectional beam events are not associated with the bow shock connection, with the exception of a few bidirectional beam events (most likely Events 10 and 15 in Table 3), which were possibly affected by the bow shock connection.

The possibility of bidirectional beams caused by the mirroring effect has been studied by many authors. For example, Lavraud et al. (2010) investigated whether counterstreaming electrons can occur inside or outside CIRs by their compressed field. To consider this possibility, we investigated the association of bidirectional beam SMFRs with a CIR, a high-speed stream (HSS), ICME, and interplanetary shock (IPS). The results are summarized in Table 3. Some of the bidirectional beam SMFR events are related to the CIR, HSS, ICME (or ejecta), or IPS. Four events (Events 3, 11, 13, and 21 in Table 3) are found to be associated with CIR (either inside or just ahead of CIR). At least four events (Events 9, 10, 15, and 16 in Table 3) are found at the leading edge of HSS. One event (Event 6 in Table 3) is found within the sheath region behind the shock driven by ICME. Two events (Events 7 and 8) are found at the trails of ICME. Furthermore, we identify three bidirectional beam events (Events 2, 12, and 14 in Table 3) that are associated with IPS but are found in the downstream region of shock. Whereas more details about the association of bidirectional beam SMFRs with solar wind conditions need to be addressed in a separate paper, here we allow the possibility that a substantial fraction of the identified bidirectional beam events are not

free of counterstreaming strahl due to reflection by either shocks or compressed magnetic regions. The schematics in Figure 11 demonstrate such situations. Thus these cases do not necessarily guarantee closed fields for SMFRs. In contrast, the remaining 11 bidirectional beam SMFRs (Events 1, 4, 5, 17–20, and 22–25 in Table 3) are found to be unrelated to any specific solar wind event, implying the high possibility that the field lines in these cases are closed.

4.3. Implications from Conic-Type Beams

Finally, we find that the peak flux of all 17 conic beam events occurs on the sunward PA side. This observation is consistent with the explanation based on the adiabatic evolution by Gosling et al. (2001) that conics arise from focusing and mirroring effects due to an open-field-line connection to magnetic field enhancements farther out in the heliosphere. They studied sunward-directed conics that occurred in conjunction with the $90°$ depletions. They suggested that conics occur far more frequently on open field lines than on closed lines when found within CMEs. In some of our conic events, the field-aligned beam flux counter to the strahl is large. For example, for four conic events (Nos. 2, 4, 8, and 14 in Table 4 and as indicated in Figure 8), we can identify a counterstreaming beam (at $\sim180°$ in Figure 8) that coexists with a stronger conic beam. Although the counterstreaming beam is much less intense than the strahl intensity, it resembles a bidirectional beam event, with the counterstreaming peak beam off the field direction. Whether these events imply a closed-field-line structure and whether scattering by waves such as whistlers (e.g., Vocks, Salem, and Lin, 2005; Pagel et al., 2007) can be a cause remain to be determined. Other than these issues, we believe that most of the conic events are associated with open field lines connected to the enhanced magnetic field region, as suggested by Gosling et al. (2001). As done for the bidirectional beam events, we checked the association of the conic events with bow shock and solar wind events, the results of which are summarized in Table 4. At least some of the conic events are associated with bow shock, CIR, HSS, and ICME.

5. Summary and Discussion

In this paper, we selected 235 SMFRs by applying a cylindrical linear force-free model fitting to a number of STs listed by Yu et al. (2016) from 20 years of Wind observations. The events published by Yu et al. were selected by the usual criteria, that is, low beta, low temperature, and enhanced magnetic field and rotation features compared to the average background conditions. To determine the global topology of SMFRs and their connectivity to the Sun, we conducted a close examination of the PA distributions of suprathermal electrons during SMFRs and determined mainly whether they are unidirectional, bidirectional, conic types, or any other type. The determination was based on both visual inspection and appropriate quantitative criteria. We found that the majority of SMFRs ($\sim45.1\%$) were accompanied by unidirectional beams (strahl). The bidirectional beams accompanied a much smaller percentage of SMFRs ($\sim10.7\%$). We also found sunward conic distributions for a small percentage of SMFRs ($\sim7.2\%$). Last, the remaining $\sim37.0\%$ of SMFRs were associated with complex electron distributions and could not be classified. The unidirectional beams and most of the conics (together corresponding to $\sim50\%$ of the total 235 SMFRs) imply open-field SMFRs with a connection to the Sun from only one end. For $\sim37.7\%$ of the unidirectional beam SMFRs, the local IMF field polarity was orthogonal or inverted (possibly due to interchange reconnection). Of them, locally inverted IMF polarity was found
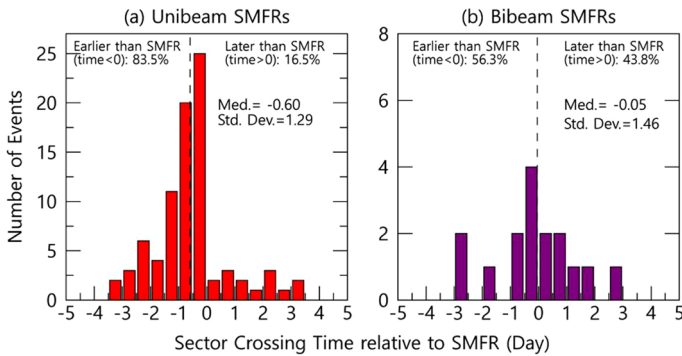
Figure 12 Distribution of sector crossing times for the unidirectional beam and bidirectional beam SMFRs. If the polarity of the IMF sector was changed earlier (later) than the SMFR event, then the time to sector crossing was described by a minus (plus) sign. The dashed line indicates the median time from SMFR to sector crossing.

for only six unidirectional beam SMFRs. Based on the solar wind conditions around the bidirectional beams, we presumed that only a very limited number of them ensured closed-field-line SMFRs.

The HCS is thought to consist of a complex exhaust embedding a succession of high-β regions and somewhat lower-β flux ropes due to sequential magnetic reconnection at the tip of the helmet streamer (Lavraud et al., 2020; Sanchez-Diaz et al., 2019). According to the suggestion, the density blobs and flux ropes are released periodically from the tip of the helmet streamers with a periodicity of 10–20 hours (Sanchez-Diaz et al., 2017a, 2017b, and 2019), in agreement with white-light observations of density blobs (e.g., Sheeley et al., 2009; Rouillard et al., 2010). As suggested by Lavraud et al. (2020), in principle, three different field topologies (accordingly accompanied by distinguished electron distributions) are possible within the flux ropes near the HCS: (i) fully disconnected fields (accompanied by strahl dropout), (ii) closed field lines anchored at the Sun at both ends (accompanied by bidirectional strahl), and (iii) open field lines anchored at the Sun at only one end in either hemisphere (accompanied by unidirectional, either parallel or antiparallel, strahl). In the previous two sections, we showed that the majority of the SMFRs studied here ($\sim$50%, revealing both the unidirectional beam and conic types) are open field lines and that only a very limited number of SMFRs (less than 10%, revealing the bidirectional beam type) are possibly closed fields. We have not identified SMFRs indicating fully disconnected fields. The open field lines might have suffered from interchange reconnection between closed magnetic loops and the adjacent open magnetic fields (Wang et al., 1998, 2000; Crooker et al., 2004), which produces transient release of material and thus contains an electron strahl population.

To check the extent to which our SMFRs may fit in the scenario of sequential blobs and flux ropes by HCS reconnection (Lavraud et al., 2020; Sanchez-Diaz et al., 2019), we estimated the sector boundary crossing times relative to each SMFR. This metric is related to the origin of SMFRs since reconnection at the sector boundary (HCS), as mentioned by Lavraud et al. (2009), could transform their field line structure to a flux rope. In this work the timing of sector crossing is defined by the times of IMF polarity reversals using 1-day windowed moving average data to remove short-lasting local variations in the IMF. The results are summarized in Figure 12 and Tables 2–4. Whereas the sector crossing time distributions differ between the unidirectional beam and bidirectional beam SMFR groups, we

hardly identified any special meaning from the difference. Nevertheless, for both groups, several cases exist where the SMFRs are found close to the nearest sector boundaries. For example, the sector crossing time is 1 day or less for 50 of the 106 unidirectional beam SM-FRs (∼47%) and 10 of the 25 bidirectional beam SMFRs (∼40%). For these SMFRs found close to the sector boundaries, we allow the possibility that the flux ropes were generated by HCS reconnection (Lavraud et al., 2020; Sanchez-Diaz et al., 2019). On the other hand, Gosling et al. (2006) suggested that HCS reconnection of open field lines at the side farther than 1 AU creates closed field lines at the sunward side and disconnected field lines at the opposite side. Then, even if these SMFRs reveal bidirectional beam electrons, the associated closed-field structure might not originate directly from the solar corona.

Feng, Zhao, and Wang (2015) investigated the counterstreaming suprathermal electron signatures of 106 SMFRs measured by Wind during 1995–2005. Feng, Zhao, and Wang (2015) found that 79 (75%) of the 106 flux ropes contained counterstreaming electrons and that the percentages of counterstreaming varied from 8% to 98%. They divided their SMFRs into two categories. One category originates from the solar corona, and most ropes are still connected to the Sun at both ends. The other category is formed near HCSs in interplanetary space. Our work is distinguished from that of Feng, Zhao, and Wang (2015) in the following aspects. First, our work is based on a larger number (by a factor of ∼2.2) of SMFRs selected from Yu et al. (2016) rather than from Feng, Zhao, and Wang (2015), whose events were based on the SMFR lists of Cartwright and Moldwin (2008) and Feng et al. (2008). Second, Feng, Zhao, and Wang (2015) based their work on a specific process (presumably, visual inspection without a quantitative criterion) of identifying counterstreaming intervals, whereas we simultaneously considered both the durations of the counterstreaming beams and their intensities relative to the strahl intensity in a quantitative way (Figures 4 and 7 and Table 3). We found that none of our 25 bidirectional beam events overlapped with the 79 counterstreaming events of Feng, Zhao, and Wang (2015). In fact, only one of their 79 counterstreaming intervals overlaps with the total event list of our work, that is, our event lists are completely different from those of Feng, Zhao, and Wang (2015). We suspect that the identification of SMFRs and associated counterstreaming electrons in Feng, Zhao, and Wang (2015) was quite different from ours. We believe that it is fair to say (as Feng, Zhao, and Wang (2015) similarly stated) that the process of identifying counterstreaming electrons is inevitably subjective to some extent, and we should not expect the exact same selection of bidirectional beam events from any two works.

Lastly, the present work is largely based on suprathermal electron data to determine the magnetic field structure of SMFRs, which is in turn related to the origin of SMFRs. In future work, additional datasets such as heavy elements should be useful to investigate possible solar origin of SMFRs as was done, for example, by Huang et al. (2017).

Declarations

References

Cartwright, M.L., Moldwin, M.B.: 2008, Comparison of small-scale flux rope magnetic properties to large-scale magnetic clouds: evidence for reconnection across the HCS? *J. Geophys. Res.* **113**, A09105. DOI.

Chen, Y., Hu, Q., Zhao, L., Kasper, J.C., Bale, S.D., Korreck, K.E., Case, A.W., Stevens, M.L., Bonnell, J.W., Goetz, K., Harvey, P.R., Klein, K.G., Larson, D.E., Livi, R., MacDowall, R.J., Malaspina, D.M., Pulupa, M., Whittlesey, P.L.: 2020, Small-scale magnetic flux ropes in the first two Parker Solar Probe encounters. *Astrophys. J.* **903**, 76. DOI.

Crooker, N.U., Huang, C.L., Lamassa, S.M., Larson, D.E., Kahler, S.W., Spence, H.E.: 2004, Heliospheric plasma sheets. *J. Geophys. Res.* **109**, A03107. DOI.

Feldman, W.C., Anderson, R.C., Asbridge, J.R., Bame, S.J., Gosling, J.T., Zwickl, R.D.: 1982, Plasma electron signature of magnetic connection to the Earth's bow shock: ISEE 3. *J. Geophys. Res.* **87**, 632. DOI.

Feng, H.Q., Zhao, G.Q., Wang, J.M.: 2015, Counterstreaming electrons in small interplanetary magnetic flux ropes. *J. Geophys. Res.* **120**, 175. DOI.

Feng, H.Q., Wu, D.J., Lin, C.C., Chao, J.K., Lee, L.C., Lyu, L.H.: 2008, Interplanetary small- and intermediate-sized magnetic flux ropes during 1995–2005. *J. Geophys. Res.* **113**, A12105. DOI.

Feuerstein, W.M., Larson, D.E., Luhmann, J.G., Lin, R.P., Kahler, S.W., Crooker, N.U.: 2004, Parameters of solar wind electron heat-flux pitch-angle distributions and IMF topologies. *Geophys. Res. Lett.* **31**, L22805. DOI.

Gosling, J.T., McComas, D.J., Skoug, R.M., Smith, C.W.: 2006, Magnetic reconnection at the heliospheric current sheet and the formation of closed magnetic field lines in the solar wind. *Geophys. Res. Lett.* **33**, L17102. DOI.

Gosling, J.T., Skoug, R.M., Feldman, W.C.: 2001, Solar wind electron halo depletions at 90° pitch angle. *Geophys. Res. Lett.* **28**, 4155. DOI.

Gosling, J.T., Teh, W.-L., Eriksson, S.: 2010, A torsional Alfvén wave embedded within a small magnetic flux rope in the solar wind. *Astrophys. J. Lett.* **719**, L36. DOI.

Gosling, J.T., Bame, S.J., Feldman, W.C., McComas, D.J., Phillips, J.L., Goldstein, B.E.: 1993, Counter-streaming suprathermal electron events upstream of corotating shocks in the solar wind beyond −2 AU: Ulysses. *Geophys. Res. Lett.* **20**, 2335. DOI.

Gosling, J.T., Skoug, R.M., Feldman, W.C., McComas, D.J.: 2002, Symmetric suprathermal electron depletions on closed field lines in the solar wind. *Geophys. Res. Lett.* **29**, 1573. DOI.

Hu, Q., Smith, C.W., Ness, N.F., Skoug, R.M.: 2004, Multiple flux rope magnetic ejecta in the solar wind. *J. Geophys. Res.* **109**, A03102. DOI.

Hu, Q., Qiu, J., Dasgupta, B., Khare, A., Webb, G.M.: 2014, Structures of interplanetary magnetic flux ropes and comparison with their solar sources. *Astrophys. J.* **793**, 53. DOI.

Hu, Q., Zheng, J., Chen, Y., Roux, J.L., Zhao, L.: 2018, Automated detection of small-scale magnetic flux ropes in the solar wind: first results from the wind spacecraft measurements. *Astron. Astrophys. Suppl. Ser.* **239**, 12. DOI.

Huang, J., Liu, Y.C.-M., Peng, J., Li, H., Klecker, B., Farrugia, C.J., Yu, W., Galvin, A.B., Zhao, L., He, J.: 2017, A multispacecraft study of a small flux rope entrained by rolling back magnetic field lines. *J. Geophys. Res.* **122**, 6927. DOI.

Kilpua, E.K.J., Luhmann, J.G., Gosling, J., Li, Y., Elliott, H., Russell, C.T., Jian, L., Galvin, A.B., Larson, D., Schroeder, P., Simunac, K., Petrie, G.: 2009, Small solar wind transients and their connection to the large-scale coronal structure. *Solar Phys.* **256**, 327. DOI.

Lavraud, B., Gosling, J.T., Rouillard, A.P., Fedorov, A., Opitz, A., Sauvaud, J.-A., Foullon, C., Dandouras, I., Génot, V., Jacquey, C., Louarn, P., Mazelle, C., Penou, E., Phan, T.D., Larson, D.E., Luhmann, J.G., Schroeder, P., Skoug, R.M., Steinberg, J.T., Russell, C.T.: 2009, Observation of a complex solar wind reconnection exhaust from spacecraft separated by over 1800 R$_E$. *Solar Phys.* **256**, 379. DOI.

Lavraud, B., Opitz, A., Gosling, J.T., Rouillard, A.P., Meziane, K., Sauvaud, J.-A., Fedorov, A., Dandouras, I., Génot, V., Jacquey, C., Louarn, P., Mazelle, C., Penou, E., Larson, D.E., Luhmann, J.G., Schroeder, P., Jian, L., Russell, C.T., Foullon, C., Skoug, R.M., Steinberg, J.T., Simunac, K.D., Galvin, A.B.: 2010, Statistics of counter-streaming solar wind suprathermal electrons at solar minimum: STEREO observations. *Ann. Geophys.* **28**, 233. DOI.

Lavraud, B., Fargette, N., Réville, V., Szabo, A., Huang, J., Rouillard, A.P., Viall, N., Phan, T.D., Kasper, J.C., Bale, S.D., Berthomier, M., Bonnell, J.W., Case, A.W., Dudok de Wit, T., Eastwood, J.P., Génot, V., Goetz, K., Griton, L.S., Halekas, J.S., Harvey, P., Kieokaew, R., Klein, K.G., Korreck, K.E., Kouloumvakos, A., Larson, D.E., Lavarra, M., Livi, R., Louarn, P., MacDowall, R.J., Maksimovic, M., Malaspina, D., Nieves-Chinchilla, T., Pinto, R.F., Poirier, N., Pulupa, M., Raouafi, N.E., Stevens, M.L., Toledo-Redondo, S., Whittlesey, P.L.: 2020, The heliospheric current sheet and plasma sheet during Parker Solar Probe's first orbit. *Astrophys. J. Lett.* **894**, L19. DOI.

Lepping, R.P., Wu, C.-C., Berdichevsky, D.B., Szabo, A.: 2011, Magnetic clouds at/near the 2007–2009 solar minimum: frequency of occurrence and some unusual properties. *Solar Phys.* **274**, 345. DOI.

Lin, R.P., Anderson, K.A., Ashford, S., Carlson, C., Curtis, D., Ergun, R., Larson, D., McFadden, J., McCarthy, M., Parks, G.K., Rème, H., Bosqued, J.M., Coutelier, J., Cotin, F., D'Uston, C., Wenzel, K.-P., Sanderson, T.R., Henrion, J., Ronnet, J.C., Paschmann, G.: 1995, A three-dimensional plasma and energetic particle investigation for the wind spacecraft. *Space Sci. Rev.* **71**, 125. DOI.

Marubashi, K., Lepping, R.P.: 2007, Long-duration magnetic clouds: a comparison of analyses using torus- and cylinder-shaped flux rope models. *Ann. Geophys.* **25**, 2453. DOI.

Moldwin, M.B., Ford, S., Lepping, R., Slavin, J., Szabo, A.: 2000, Small-scale magnetic flux ropes in the solar wind. *Geophys. Res. Lett.* **27**, 57. DOI.

Nishimura, N., Marubashi, K., Tokumaru, M.: 2019, Comparison of cylindrical interplanetary flux-rope model fitting with different boundary pitch-angle treatments. *Solar Phys.* **294**, 49. DOI.

Owens, M.J., Crooker, N.U., Lockwood, M.: 2013, Solar origin of heliospheric magnetic field inversions: evidence for coronal loop opening within pseudostreamers. *J. Geophys. Res.* **118**, 1868. DOI.

Pagel, C., Gary, S.P., de Koning, C.A., Skoug, R.M., Steinberg, J.T.: 2007, Scattering of suprathermal electrons in the solar wind: ACE observations. *J. Geophys. Res.* **112**, A04103. DOI.

Philips, J.L., Gosling, J.T.: 1990, Radial evolution of solar wind thermal electron distributions due to expansion and collisions. *J. Geophys. Res.* **95**, 4217. DOI.

Réville, V., Velli, M., Rouillard, A.P., Lavraud, B., Tenerani, A., Shi, C., Strugarek, A.: 2020, Tearing instability and periodic density perturbations in the slow solar wind. *Astrophys. J. Lett.* **895**, L20. DOI

Rouillard, A.P., Savani, N.P., Davies, J.A., Lavraud, B., Forsyth, R.J., Morley, S.K., Opitz, A., Sheeley, N.R., Burlaga, L.F., Sauvaud, J.-A., Simunac, K.D.C., Luhmann, J.G., Galvin, A.B., Crothers, S.R., Davis, C.J., Harrison, R.A., Lockwood, M., Eyles, C.J., Bewsher, D., Brown, D.S.: 2009, A multispacecraft analysis of a small-scale transient entrained by solar wind streams. *Solar Phys.* **256**, 307. DOI.

Rouillard, A.P., Lavraud, B., Davies, J.A., Savani, N.P., Burlaga, L.F., Forsyth, R.J., Sauvaud, J.-A., Opitz, A., Lockwood, M., Luhmann, J.G., Simunac, K.D.C., Galvin, A.B., Davis, C.J., Harrison, R.A.: 2010, Intermittent release of transients in the slow solar wind: 2. In situ evidence. *J. Geophys. Res.* **115**, A04103. DOI.

Rouillard, A.P., Sheeley, N.R. Jr, Cooper, T.J., Davies, J.A., Lavraud, B., Kilpua, E.K.J., Skoug, R.M., Steinberg, J.T., Szabo, A., Opitz, A.: 2011, The solar origin of small interplanetary transients. *Astrophys. J.* **734**, 7. DOI.

Sanchez-Diaz, E., Rouillard, A.P., Davies, J.A., Lavraud, B., Sheeley, N.R., Pinto, R.F., Kilpua, E.K.J.: 2017a, The temporal and spatial scales of density structures released in the slow solar wind during solar activity maximum. *Astrophys. J.* **851**, 32. DOI.

Sanchez-Diaz, E., Rouillard, A.P., Davies, J.A., Lavraud, B., Pinto, R.F., Kilpua, E., Plotnikov, I., Genot, V.: 2017b, Observational evidence for the associated formation of blobs and raining inflows in the solar corona. *Astrophys. J.* **835**, L7. DOI.

Sanchez-Diaz, E., Rouillard, A.P., Lavraud, B., Kilpua, E., Davies, J.A.: 2019, In situ measurements of the variable slow solar wind near sector boundaries. *Astrophys. J.* **882**, 51. DOI.

Sheeley, N.R. Jr., Lee, D.D.-H., Casto, K.P., Wang, Y.-M., Rich, N.B.: 2009, The structure of streamer blobs. *Astrophys. J.* **694**, 1471. DOI.

Shimazu, H., Vandas, H.: 2002, A self-similar solution of expanding cylindrical flux ropes for any polytropic index value. *Earth Planets Space* **54**, 783. DOI.

Stansberry, J.A., Gosling, J.T., Thomsen, M.F., Bame, S.J., Smith, E.J.: 1988, Interplanetary magnetic field orientations associated with bidirectional electron heat fluxes detected at ISEE 3. *J. Geophys. Res.* **93**, 1975. DOI.

Vocks, C., Salem, C., Lin, R.P.: 2005, Electron halo and strahl formation in the solar wind by resonant interaction with whistler waves. *Astrophys. J.* **627**, 540. DOI.

Wang, Y.-M., Sheeley, N.R. Jr., Walters, J.H., Brueckner, G.E., Howard, R.A., Michels, D.J., Lamy, P.L., Schwenn, R., Simnett, G.M.: 1998, Origin of streamer material in the outer corona. *Astrophys. J.* **498**, L165. DOI.

Wang, Y.-M., Sheeley, N.R. Jr., Socker, D.G., Howard, R.A., Rich, N.B.: 2000, Electron halo and strahl formation in the solar wind by resonant interaction with whistler waves. *J. Geophys. Res.* **105**, 25133. DOI.

Wimmer-Schweingruber, R.F., Crooker, N.U., Balogh, A., Bothmer, V., Forsyth, R.J., Gazis, P., Gosling, J.T., Horbury, T., Kilchenmann, A., Richardson, I.G., Richardson, J.D., Riley, P., Rodriguez, L., von Steiger, R., Wurz, P., Zurbuchen, T.H.: 2006, Understanding interplanetary coronal mass ejection signatures. *Space Sci. Rev.* **123**, 177. DOI.

Yu, W., Farrugia, C.J., Lugaz, N., Galvin, A.B., Kilpua, E.K.J., Kucharek, H., Möstl, C., Leitner, M., Torbert, R.B., Simunac, K.D.C., Luhmann, J.G., Szabo, A., Wilson, L.B. III, Ogilvie, K.W., Sauvaud, J.-A.: 2013, The magnetic field geometry of small SolarWind flux ropes inferred from their twist distribution. *J. Geophys. Res.* **119**, 689. DOI.

Yu, W., Farrugia, C.J., Lugaz, N., Galvin, A.B., Möstl, C., Paulson, K., Vemareddy, P.: 2016, The magnetic field geometry of small solar wind flux ropes inferred from their twist distribution. *Solar Phys.* **293**, 165. DOI.

Zeng, J., Hu, Q.: 2018, Observational evidence for self-generation of small-scale magnetic flux ropes from intermittent solar wind turbulence. *Astrophys. J.* **852**, L23. DOI.

Zhao, L.-L., Zank, G.P., Adhikari, L., Hu, Q., Kasper, J.C., Bale, S.D., Korreck, K.E., Case, A.W., Stevens, M., Bonnell, J.W., Dudok de Wit, T., Goetz, K., Harvey, P.R., MacDowall, R.J., Malaspina, D.M., Pulupa, M., Larson, D.E., Livi, R., Whittlesey, P., Klein, K.G.: 2020a, Dentification of magnetic flux ropes from Parker Solar Probe observations during the first encounter. *Astron. Astrophys. Suppl. Ser.* **246**, 26. DOI.

Zhao, L.-L., Zank, G.P., Hu, Q., Telloni, D., Chen, Y., Adhikari, L., Nakanotani, M., Kasper, J.C., Huang, J., Bale, S.D., Korreck, K.E., Case, A.W., Stevens, M., Bonnell, J.W., Dudok de Wit, T., Goetz, K., Harvey, P.R., MacDowall, R.J., Malaspina, D.M., Pulupa, M., Larson, D.E., Livi, R., Whittlesey, P., Klein, K.G., Raouafi, N.E.: 2020b, Detection of small magnetic flux ropes from the third and fourth Parker Solar Probe encounters. *Astron. Astrophys.* DOI. arXiv.